

Additive Manufacturing of Cu on 316L Stainless Steel via Inconel 718 Intermediate Layers

Xinchang Zhang ^{1,2,*}, Tan Pan ², Yitao Chen ², Frank Liou ²

¹ Idaho National Laboratory, Idaho Falls, Idaho, 83401, USA

² Department of Mechanical & Aerospace Engineering, Missouri University of Science and
Technology, Rolla, Missouri, 65409, USA

* Corresponding author: xinchang.zhang@inl.gov

Abstract

Joining of dissimilar materials is becoming increasingly prevalent to combine differing material properties to enhance product design flexibility and performance. In this study, pure copper was built on 316L stainless steel (SS316L) by laser-based additive manufacturing technology in which copper was deposited layer-by-layer on SS316L with Inconel 718 intermediate layers. The goal is to fabricate multi-metallic structures with improved thermal conductivity. The direct joining of Cu on SS316L would result in porosities at the interface and the consequent poor mechanical properties, which could be addressed by Inconel 718 intermediate layers. The microstructure, chemical composition, tensile properties, and micro-hardness were characterized in the dissimilar materials using scanning electron microscopy, energy dispersive spectroscopy, tensile test with digital image correlation technique, and hardness tester. Results confirm excellent bonding when Inconel 718 intermediate layers are introduced.

Keywords: Additive Manufacturing; Functionally Graded Materials; Cu; Stainless Steel; Dissimilar materials

Introduction

Many metallic components in modern systems are frequently subjected to a complex and diverse working environment. For example, a jet engine has a large number of parts that are subjected to severe working conditions including high temperature, high pressure, corrosion, strong centrifugal load, etc. [1]. Meanwhile, the working condition is location-dependent, which indicates different parts can experience varied conditions. Therefore, a single part that has location-dependent composition and thus properties is highly desired in future advanced systems to offer distinct properties within the single part, which can better fulfill the design requirements [2]. Such a desire promotes the design and fabrication of functionally graduated materials (FGM). FGM is a novel material that features different compositions in different positions, resulting in corresponding changes in the properties in terms of mechanical, thermal, electrical, chemical, etc. FGM has the benefits to combine the strength of each material and thus provide a unique solution for the design of components that need to work in a complex environment.

With the emerge of many advanced manufacturing techniques, the fabrication of FGM becomes possible. Among these advanced manufacturing techniques, additive manufacturing (AM) is a preferred choice for making FGM due to its fabrication nature. According to the American Society for Testing and Materials (ASTM) F2792-12a, AM can be classified into seven categories based on the manufacturing principle [2]. Many of these technologies are particularly being

investigated, such as powder bed fusion (PBF), binder jetting, and directed energy deposition (DED). For the fabrication of FGM structures, DED is particularly suitable. In the DED process, materials in the form of powder or wire are deposited on a substrate according to a designed tool path. The shape of an object is obtained in a layer-by-layer fashion, which is opposite to the traditional machine process where materials are cut from a block. Since materials are added layer upon layer, the material composition can be changed as a function of layer by easily changing the feedstock material. The material composition can even be changed as a function of a spot within a single layer. Such flexibility makes DED widely used to fabricate FGM structures. Based on engineering needs, a wide type of FGM has been designed and made by AM. For instance, Li et al. designed and fabricated Ti6Al4V-SS316L (stainless steel 316L) FGM to combine the high strength-to-weight ratio and high-temperature strength/toughness of Ti6Al4V with the corrosive resistance and low cost of SS316L [3]. A special grading route Ti6Al4V → V → Cr → Fe → SS316L was designed to eliminate the formation of detrimental brittle phases. Inconel 625 was joined with SS316L to take advantage of the high strength at elevated temperatures which Inconel 625 can provide and good machinability and lower price which SS316L can provide [4]. Many other types of FGM have been reported including Inconel 718 – GPCop 84 copper [5], Ti6Al6V-Invar [6], SS304L-Inconel 625 [6], and H13 tool steel – copper [7].

Joining copper with stainless steel (SS) to create copper-SS FGM is very attractive due to the wide application of this structure. Copper is known for its very high thermal and electrical conductivity. Therefore, joining copper with SS can simultaneously use the high thermal conductivity of copper and the high strength and corrosion resistance of SS. Such a hybrid structure can be used in places where efficient cooling is desired, such as in power generation industries, nuclear industries, heat exchangers, die casting parts, etc [8]. Traditionally, copper was joined with SS by the welding process, such as explosive welding [9], laser welding [10], and diffusion welding [11]. It should be noted that since copper and stainless steel have significant dissimilarities in physical, chemical, and thermo-mechanical properties, joining copper with stainless steel is a challenging task. It is reported that Fe and Cu have very limited solid solubility [12]. In addition, high residual stress can be built up in the welding interface, which can cause cracking [13]. Previous studies have reported the failure in joining copper with stainless steel due to the aforementioned drawbacks [14][15][16][17].

This study aims to investigate the feasibility of fabricating copper-SS FGM structures using additive manufacturing. Due to the crack-prone phenomenon in the direct joining of copper on SS, intermediate layers made of Inconel 718 (IN718) was added between copper and SS. IN718 has a high content of element Ni and since Ni can form a solid solution with Cu, it is expected that the final FGM is defect-free. In this study, SS316L was deposited first, followed by the deposition of IN718 on SS316L, and finally followed by the deposition of copper on IN718. The resulting structure was characterized in terms of microstructure, elemental distribution, tensile properties, and hardness distribution. The outcome of this study provides an innovative solution to join copper with stainless steel using additive manufacturing techniques to enhance the overall performance of the FGM structure.

Feedstock Materials and Experimental Setup

SS316L, IN718, and Cu powder materials were provided as the feedstock. The SS316L and IN718 powders were procured from Carpenter Technology Corporation. The Cu powder was supplied by Royal Metal Powders Inc. All three types of powders were fabricated by the gas optimization process. Figures 1a, 1b, and 1c depict the scanning electron microscopy (SEM) images of SS316L, IN718, and Cu powder, respectively. As can be seen, the micro-topographies of these three types of powders are spherical while some tiny satellite particles are scarcely found and attached to major large particles. ImageJ software was used to characterize the particle size and distribution of the powders. As can be seen in Figures 1d, 1e, and 1f, these three types of powders are featured with normal distribution with an average particle diameter of 116 μm for SS316L, 79 μm for IN718, and 110 μm for Cu powder. The chemical composition of SS316L, IN718, and Cu powder feedstock was provided by the powder manufacturers and the composition is displayed in Table 1. SS304L rectangular blocks were utilized as the substrate. Table 1 also presents the composition of SS304L as the substrate material. Table 2 lists the physical and thermal properties of Cu, IN718, SS316L, and SS304L.

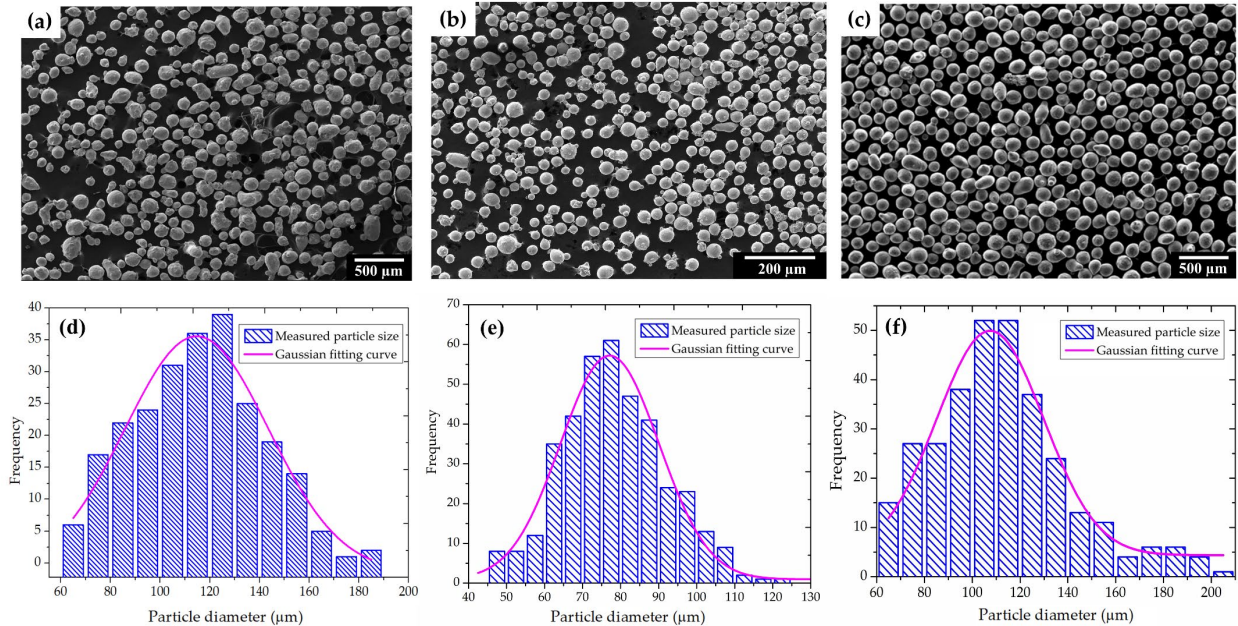


Figure 1. Microscopic morphology of (a) SS316L powder, (b) IN718 powder, and (c) Cu powder; Particle size distribution of the (d) SS316L, (e) IN718, and (f) Cu powder.

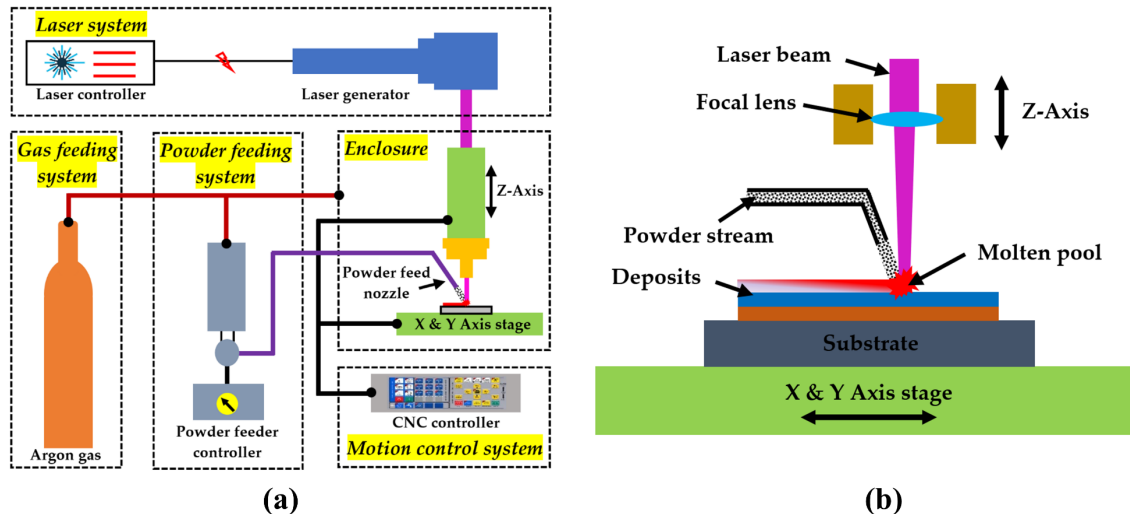
Table 1. Chemical composition of SS304L, SS316L, D22 and Cu (wt.%)

Materials	Fe	Cr	Ni	Mn	Mo	Nb	P	S	Si	N	C	B	Cu
SS304L	Bal.	19	11	1.62	-	-	0.02	0.01	0.50	0.07	0.02	-	-
SS316L	Bal.	17	12	1.8	2.5	-	0.03	0.02	0.5	0.05	0.02	-	-
IN718	Bal.	18.5	53.4	0.03	3	5.3	-	-	0.07	-	0.02	1.4	0.03
Cu	-	-	-	-	-	-	-	-	-	-	-	-	>99.99

Table 2. Physical and thermal properties of SS304L, SS316L, IN718, and Cu

	SS304L	SS316L	IN718	Cu
Density (g/cm ³)	8.03	7.99	8.17	8.96
Melting point (°C)	1399-1454	1375-1400	1260-1336	1085
Thermal conductivity (W/m-K)	14.0	13.6	11.4	400
Thermal expansion coefficient ($\times 10^{-6}/^{\circ}\text{C}$)	17.3	14.8	13.4	17

The schematic diagram of the DED system used in this experiment is presented in Figure 2a. The complete DED equipment consists of a laser system, gas feeding system, powder feeding system, deposition enclosure, and control system. The laser source is a Yb-fiber (IPG YLR-1000, USA) laser with a 1 kW maximum power, 1064 nm wavelength, and 2 mm beam diameter. The energy distribution of the circular laser beam follows the Gaussian profile. The relative movement between the laser head and deposition platform is realized by a 3-axis stage. An electrostatic powder feeder (X2 powder feed system from Powder Motion Labs, USA) was used in this study for material feeding. Argon is utilized as the carrier gas to deliver powder particles from the powder feeder to the molten pool. Argon is also used as shielding gas in the deposition enclosure to prevent materials from oxidation. All DED components were controlled by a customized computer numerical control (CNC) software developed in Linux. The DED deposition principle is schematically illustrated in Figure 2b. The laser beam is in the vertical direction and the powder feed nozzle is 20° tilted from the laser beam. The distance from the end of the powder nozzle to the top surface of the substrate is 15 mm. During deposition, the laser beam creates a molten pool on a substrate. Meanwhile, powders are transported into the molten pool, melted, and then solidified to form a laser. This process continues so that the designed 3D shape can be formed.

**Figure 2.** Schematic of (a) DED equipment and (b) deposition process.

The multi-metallic structure as presented in Figure 3a was fabricated in this investigation. First, an SS316L thin-wall structure with a length of 36 mm and a height of 8 mm was deposited on an SS304L substrate. The layer thickness is set as a constant value of 0.5 mm. The deposition

tool path is a single-track multi-layer pattern as inserted in Figure 3a. Materials were deposited in both forward and backward directions with no interlayer dwell. This tool path was also applied to the deposition of IN718 and Cu as discussed below. Once the SS316L and substrate were cooled to room temperature. Next, IN718 was deposited on the top of SS316L. The part was cooled down to room temperature again before the deposition of Cu on the top of IN718. The detailed processing parameters are given in Table 3.

Table 3. DED processing parameters for fabricating the SS-IN718-Cu FGM

Parameter	SS-IN718-Cu FGM		
	SS316L	IN718	Cu
Laser power (W)	600	500	550
Laser beam size (mm)	2	2	2
Scan speed (mm/min)	210	210	210
Layer thickness (mm)	0.5	0.4	0.3
Number of layers	16	6	16
Deposit length (mm)	36	36	36
Deposit height (mm)	8	2.4	4.8

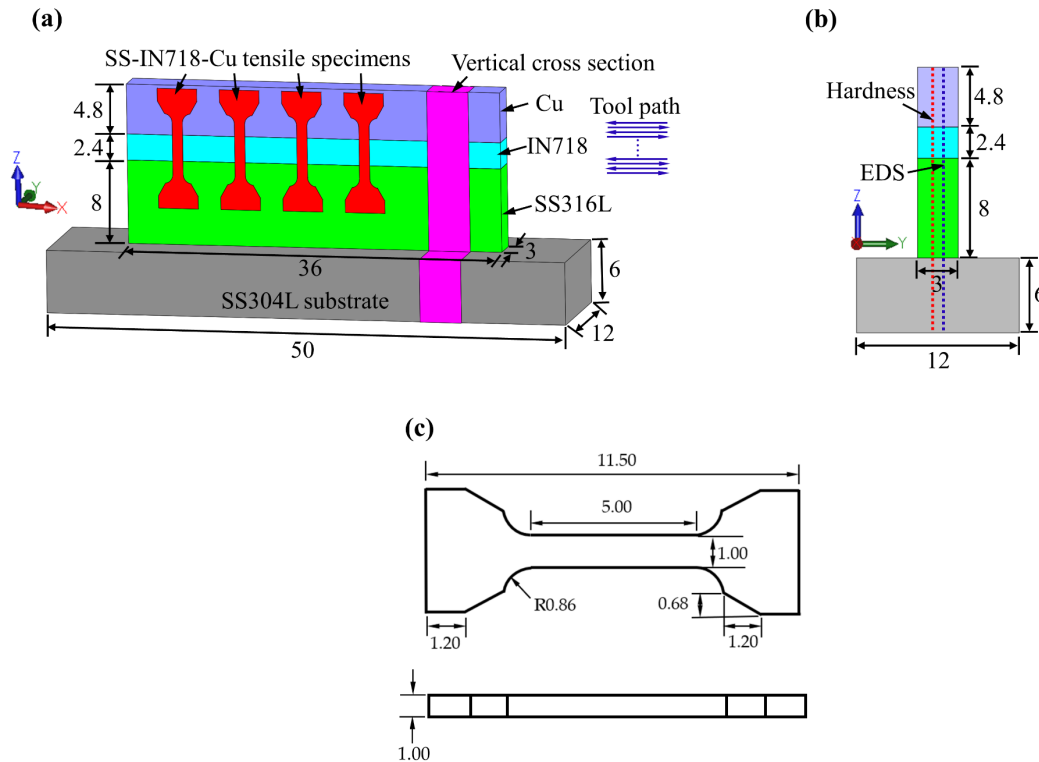


Figure 3. (a) Schematic of SS-IN718-Cu FGM; (b) Sectioned vertical cross-section; (c) Dimensions of tensile test specimens (all dimensions are in mm).

A vertical cross-section was sectioned from the as-fabricated structure as shown in Figure 3b. The cut piece was mounted on conductive Bakelite. After that, the sample was ground using silicon carbide abrasive papers from 120 grit to 1200 grit in sequence, polished using 9 μm , 6 μm , 3 μm , and 1 μm diamond suspension, and finally polished using 0.02 μm silica suspension. The

sample was ultrasonically cleaned immediately after polishing. Since the microstructure of different materials is of interest, different etchants were selected. In order to show the microstructure of IN718 and SS316L, the sample was firstly electrolytically etched with 10% oxalic acid under 2V for 30 seconds. After that, the sample was etched using a solution of 70% ethanol, 25% hydrochloric acid, and 5% ferric chloride by immersion for 15 seconds to reveal the microstructure of the Cu. The prepared sample was analyzed using scanning electron microscopy (SEM, FEI Helios NanoLab 600 Dual Beam) coupled with an Oxford Energy Dispersive X-ray Spectroscopy (EDS). EDS mapping was carried out on the SS-IN718-Cu FGM to study elemental diffusion across the interface of dissimilar materials.

In order to reveal the mechanical properties of the SS-IN718-Cu FGM, tensile specimens were prepared from the as-fabricated sample as illustrated in Figure 3a. Tensile specimens were cut in the vertical direction. The dimensions of tensile specimens are shown in Figure 3c. The tensile gauge section consists of three materials (SS, IN718, and Cu). Therefore, tensile testing of these samples can reveal the bonding strength between dissimilar materials. The tensile specimens were tested using an Instron universal testing machine with a crosshead speed of 0.15 mm/min. *In-situ* digital image correlation (DIC) technique was used to show the strain maps during the tensile test. The longitudinal surface of the fractured sample was analyzed using SEM to study the region of fracture. Vickers microhardness test was also performed on the SS-IN718-Cu FGM to investigate hardness profile across different layers. Vickers microhardness measurements were carried out along the vertical building direction using a Struers Druamin-5 hardness tester with a load of 4.9 N and a hold time of 10 seconds. Three measurements were conducted at the same height, and the average value and standard deviation were reported.

Results and Discussion

Microstructure

The microstructure of the SS-IN718-Cu FGM at different locations is shown in Figure 4. As can be seen from Figure 4a, the SS316L layers were dominated by columnar dendrites. This columnar structure was widely reported previously in the as-deposited SS316L materials both manufactured by directed energy deposition [18] and selective laser melting process [19]. In SS316L deposits close to the substrate, columnar dendrites usually grow in the vertical direction. This is because the temperature gradient is significant in the vertical direction, causing the dendrites to elongate in this direction. With the increase of layers, SS316L tends to transform to a mixture of columnar dendrites and equiaxed structures. This variation of microstructure in different layers of additively manufactured SS316L can be explained by the solidification theory [20]. In the solidification process, the solidification velocity (V) and temperature gradient (G) are important parameters to guide microstructure formation. With the reduction of G/V , the microstructure can change from planar to dendrite and finally to an equiaxed structure. At the beginning of the deposition process (initial layer), the temperature of the substrate is relatively low. This can result in a very high temperature gradient between the as-deposited layers and substrate. It is reported that this temperature gradient G can reach up to 8×10^5 K/m in the deposition of SS316L [21]. Therefore, the G/V ratio can be as high as 900 – 6000 Ks/mm² as reported in [22]. This extremely high G/V ratio caused the formation of columnar dendrites in the vertical direction in the lower SS316L layers. With the increase of layers, the temperature gradient between the

newly deposited layer and the layer underneath is reduced. Since a relatively low G/V was achieved in the upper layers, the upper layers are featured with a mixture of columnar and equiaxed structures.

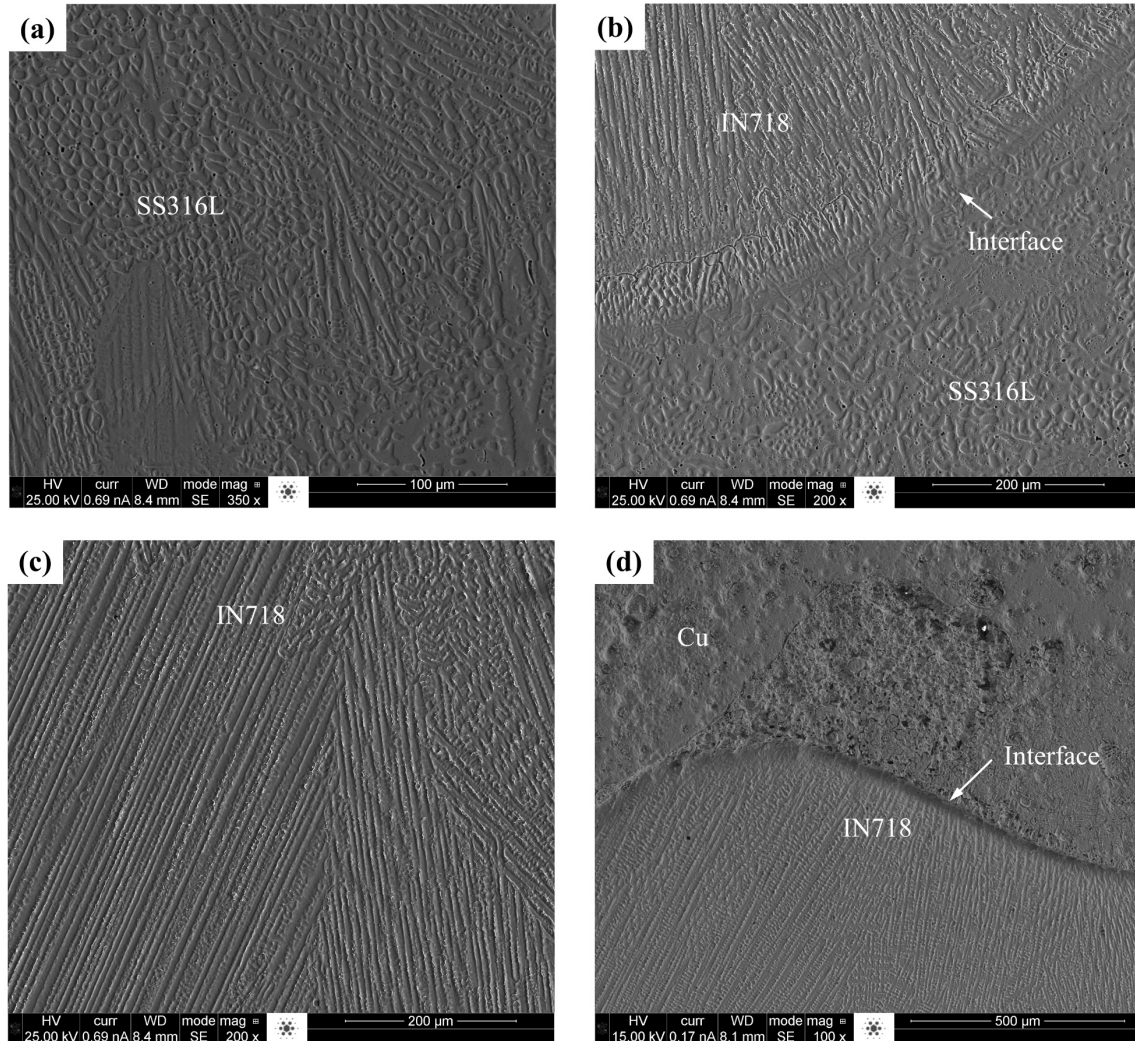


Figure 4. Microstructure of (a) SS316L close to the substrate, (b) IN718-SS316L transition zone, (c) middle layer of IN718, and (d) Cu-IN718 transition zone.

Figure 4b shows the microstructure at the SS316L and IN718 transition zone. In terms of defects, no defects such as delamination or pores were identified in the interface. The microstructure at the transition zone shows a good bonding between SS316L and IN718. SS316L and IN718 are both fcc (face-centered cubic) austenite structures. Based on the Fe-Ni phase diagram as seen in Figure 5a, a large window with no detrimental intermetallic can be achieved. It is expected that a solid bonding can be obtained between SS316L and IN718, which can be validated by the microstructure analysis in Figure 4b and mechanical testing discussed in the following of this paper. In terms of microstructure, the IN718 featured with different structure when compared with the SS316L below the interface, as can be seen in Figure 4b. Such difference

in microstructure can also be explained by the solidification mechanism discussed above. As mentioned in the experimental procedure section, the as-deposited SS16L and substrate were cooled down to room temperature before the deposition of IN718. Therefore, in the deposition of the first layer of IN718, the G/V is extremely high, causing the formation of columnar structure in the direction where the temperature gradient is the highest. The microstructure of IN718 in the middle layer also reveals dominated columnar dendrites (Figure 4c). Since the IN718 was deposited as intermediate layers with a total layer number of 6, it is reasonable to expect that the G/V is still high in the middle and upper IN718 layers, resulting in the columnar dendritic structure.

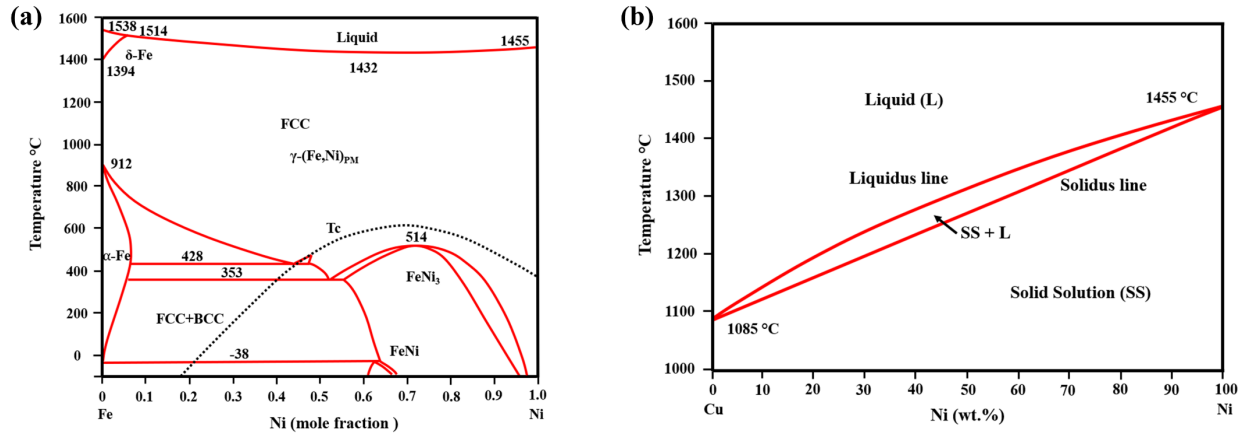


Figure 5. Phase diagrams for (a) Fe-Ni and (b) Cu-Ni system.

Figure 4d shows the microstructure at the IN718-Cu transition zone. The micrograph confirms that the IN718-Cu interface is defect-free. A good interfacial bonding strength can be expected (validated by tensile testing below). Since the Cu was >99.99 % pure, no obvious structure was observed in the bulk Cu deposits. However, the deposits close to the interface featured unevenly distributed composition and structure as can be seen in Figure 4d. This has resulted from the diffusion of composition from the IN718 layers to the layers above the interface. Such phenomenon is discussed below supported by EDS data.

Figure 6 shows the EDS maps over the IN718-Cu transition zone. It reveals that above the interface, Cu is the dominant content which is expected. However, areas, where IN718 was rich, can also be found. This shows that the IN718 composition penetrated the Cu layers. A gradual transition of composition across the interface was observed due to large elemental diffusion. This chemical dilution is common in additively manufactured multi-material structures. In the additive manufacturing process, when the lower material is melted (IN718 in this study), the incoming new material (Cu in this study) is delivered into the melt pool and mixed with the existing material. When the material is solidified, a composition of the lower material can be found in the newly deposited layers. In the additive manufacturing process, the Marangoni convection happens in the molten pool. The thermal Marangoni convection is positively proportional to surface tension and temperature gradient. In the deposition of Cu on IN718, the center of the molten pool has a higher temperature than the edge. This temperature difference causes a surface tension gradient toward the edge of the molten pool. Therefore, the lower material is pulled into the upper location. In this study, the pure Cu has a very high thermal conductivity, which can cause intensified dynamics of the Marangoni convection in the molten pool. Such intensified Marangoni convection caused the

large dilution of IN718 into the Cu layers. It should be mentioned that large interfacial dilution is helpful for residual stress mitigation since the discrepancy between two distinct materials was wakened [23].

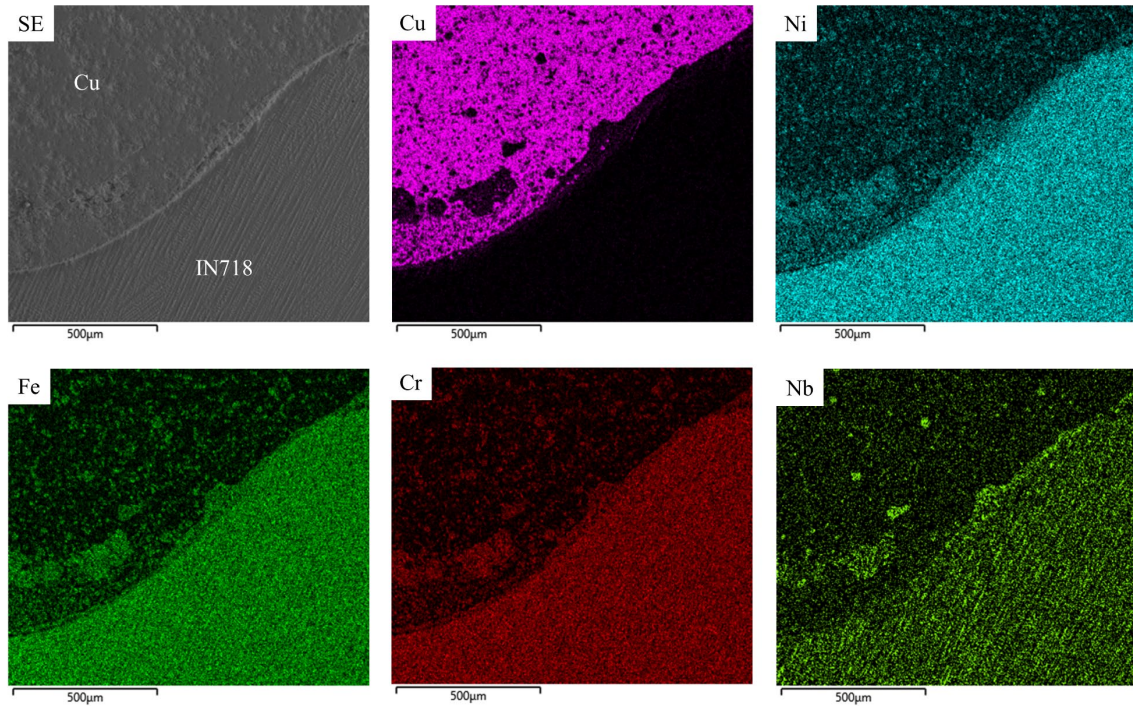


Figure 6. Elemental mapping over Cu-IN718 transition zone.

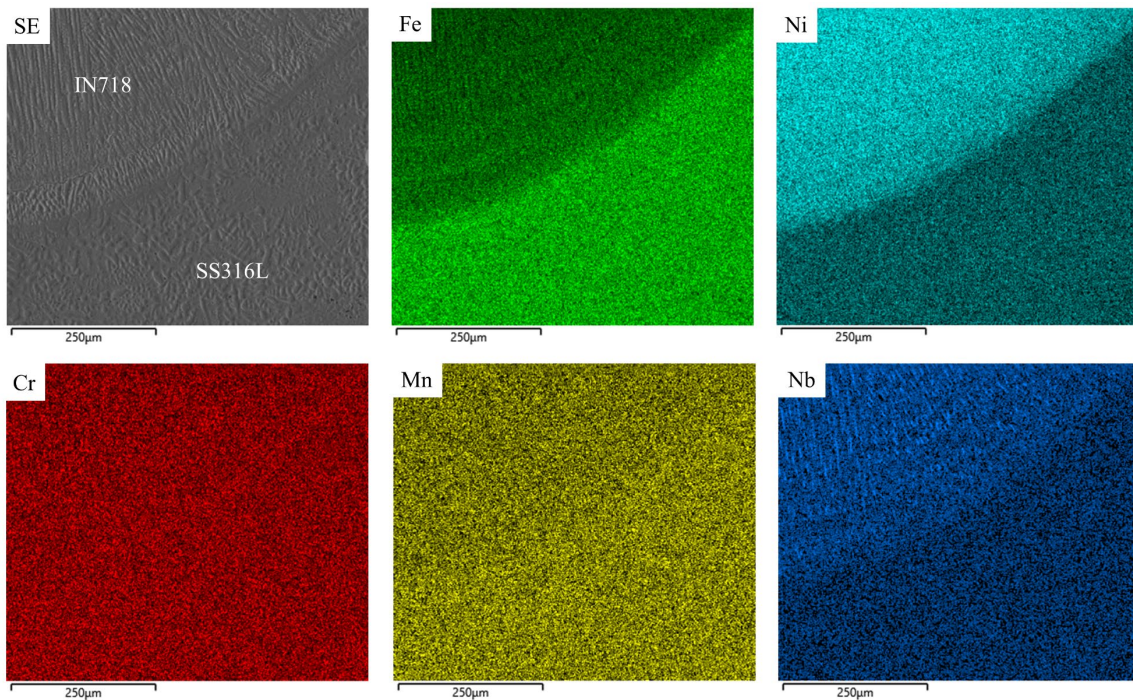


Figure 7. Elemental mapping over IN718-SS316L transition zone.

Figure 7 shows the EDS maps across the SS-IN718 transition zone. An interface where the material starts to change can be seen. The material below the interface is rich in Fe, aligned with the fact that more Fe in SS316L. The Cr composition is similar above and below the interface since very close of Cr composition in SS316L and IN718, as can be seen in Table 1.

Tensile Properties

As illustrated in Figure 3a, each tensile specimen has the as-deposited Cu, IN718, and SS316L. Tensile testing of the specimens can provide an understanding of the bonding strength between dissimilar materials. Figure 8 presents a representative tensile stress-strain curve. Table 4 summarizes the 0.2% offset yield strength (YS) and ultimate tensile strength (UTS) of this study compared with existing data. The result shows the average YS and UTS are 155 ± 7 MPa and 257 ± 25 MPa, respectively. Figure 9 shows the *in-situ* DIC strain field at different stages in the testing of the specimen. DIC result shows that deformation has mostly happened at the Cu section, which is expected since the strength of Cu is the lowest among the Cu, IN718, and SS316L. The low tensile strength was not able to cause significant deformation over the IN718 and SS316L regions. All the tensile specimens fractured at the Cu region, demonstrating the bonding strength of the multi-material system is higher than the UTS of the Cu. Table 4 lists the previously reported tensile properties of pure or almost pure Cu made of additive manufacturing or traditional process techniques. The data shows the tensile strength of the Cu made in this study is comparable to the literature data.

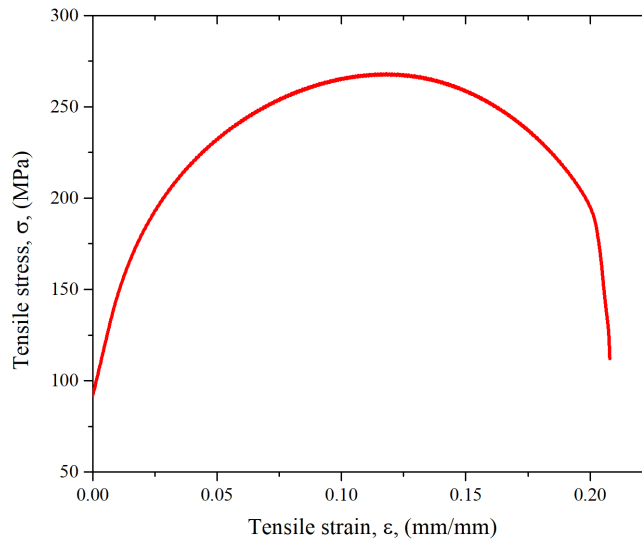


Figure 8. Stress-strain curve of Cu-IN718-SS316L FGM.

Table 5. Comparison of tensile properties obtained in this study to reference values

Material and reference	Technique	YS (MPa)	UTS (MPa)
>99.9 wt.% Cu, this study	DED	155±7	257±25
>99.2 wt.% Cu, [24]	SLM	n/a	195 (parallel) 210 (vertical)
>99.2 wt.% Cu, [25]	SLM	n/a	49±10 (pores, unmelted particles)
>94.9 wt.% Cu, [26]	BJ	n/a	117 (porosity)
CP copper, [27]	CS	n/a	125
>99.9 wt.% Cu, [28]	MFAM	140	220
>99.5 wt.% Cu, [29]	Hot rolled	110	260

DED: directed energy deposition; SLM: selective laser melting; BJ: binder jetting; CS: cold spray; MFAM: metal foil AM;

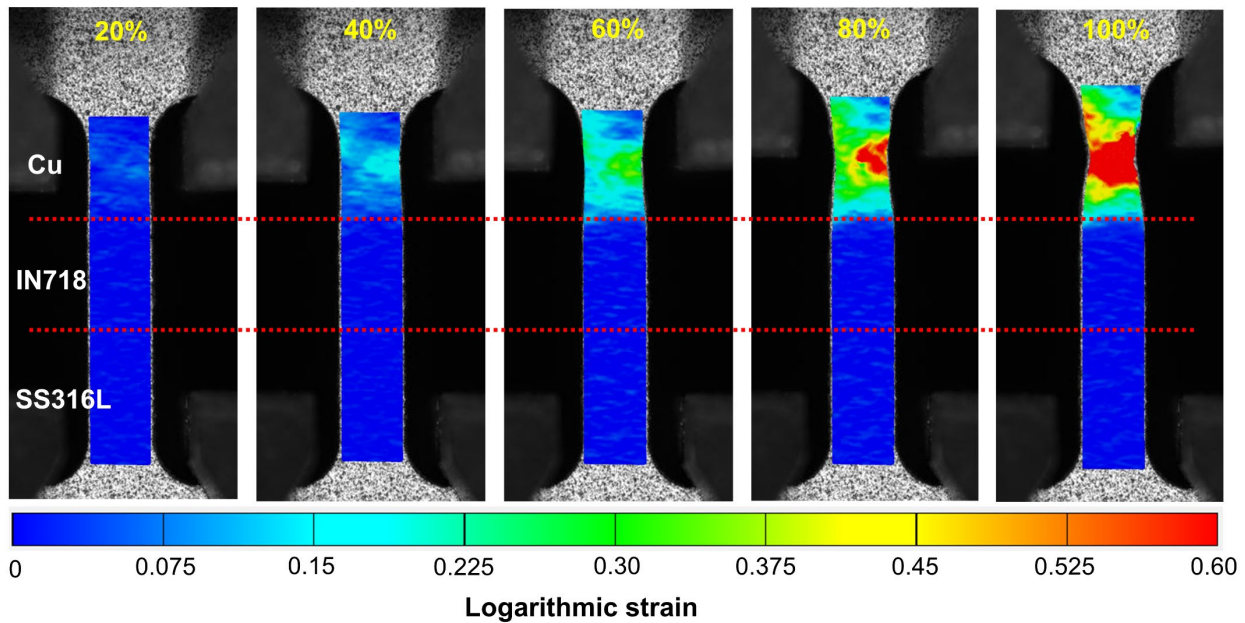


Figure 9. In-situ DIC strain field during tensile testing of Cu-IN718-SS316L specimens (percent indicates strain percentage).

Vickers Hardness

The microhardness was measured from the substrate to the as-deposited Cu along the vertical building direction. Figure 10 shows the hardness profile. The measurement reveals that the as-fabricated SS316L featured a hardness of 173 ± 6 HV. This is a typical value compared with SS316L made by additive manufacturing [30]. When reaching the IN718 region, the hardness shows a gradual increase. It can be seen that since elemental diffusion occurred in the IN718-SS transition zone, the hardness shows a gradual increase with the distance approaching the IN718 region. The as-deposited IN718 has a maximum hardness of 253 HV at approximately the middle of the IN718 layers. This is because of the composition dilution at the SS-IN718 and IN718-Cu transition zones, which weakened the hardness of IN718. Extending to the Cu region, a gradual

drop of hardness is seen. Since Ni can form a solid solution with Cu (Figure 5b), the diffusion of IN718 into the Cu layers is significant, causing the gradual decrease of hardness. The Cu upper layers have a roughly stabilized hardness of 70 HV.

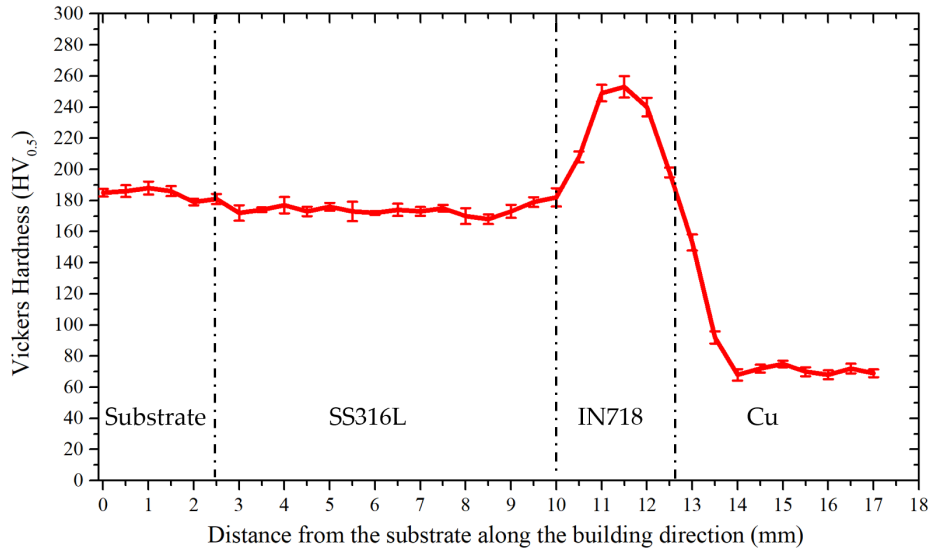


Figure 10. Hardness distribution along the building direction of the SS-IN718-Cu FGM.

Conclusion

This study investigated the fabrication of functionally graded structures by joining pure copper with stainless steel via Inconel 718 intermediate layers by an additive manufacturing process. The ultimate goal of this study is to combine the excellent thermal conductivity of copper with the high strength and corrosion resistance of stainless steel for applications where efficient cooling is required. In the present work, the SS316L-IN718-Cu FGM structure has been successfully fabricated. The final FGM structure was evaluated in microstructure, tensile properties, and microhardness distribution. The primary findings are:

- (1) Defect-free FGM structure has been achieved by inserting IN718 interlayers between SS316L and pure copper. IN718 intermediate layers successfully eliminated the cracking issue in the direct joining of SS316L with copper.
- (2) A transition of microstructure was observed along the building direction. This change of microstructure can be explained by the solidification theory guided by the change of G/V . Columnar grains dominated the lower SS316L layers while the upper SS316L layers have a mixture of columnar and equiaxed structure. The IN718 layers are dominated by columnar structure.
- (3) Elemental diffusion happens across both the SS-IN718 and IN718-Cu interfaces. This extended elemental diffusion is due to the Marangoni convection in the molten pool.
- (4) The YS and UTS of the SS316L-IN718-Cu structure are 155 ± 7 MPa and 257 ± 25 MPa, respectively. The FGM structure fractured at the Cu region while the interfaces are survived, indicating the bonding strength is higher than the UTS of the FGM.

- (5) A change of hardness is observed along the building direction due to material differences. Hardness varies smoothly across the interfaces due to large elemental dilution.

Conclusion

This project was supported by National Science Foundation Grants CMMI-1547042 and CMMI 1625736, Intelligent Systems Center, Center for Aerospace Manufacturing Technologies, and Material Research Center at Missouri S&T. Their financial support is greatly appreciated.

References

- [1] X. Zhang, W. Li, F. Liou, Damage detection and reconstruction algorithm in repairing compressor blade by direct metal deposition, *Int. J. Adv. Manuf. Technol.* 95 (2018) 2393–2404. <https://doi.org/10.1007/s00170-017-1413-8>.
- [2] X. Zhang, F. Liou, Chapter 1 - Introduction to additive manufacturing, in: J. Pou, A. Riveiro, J.P.B.T.-A.M. Davim (Eds.), *Handbooks Adv. Manuf.*, Elsevier, 2021: pp. 1–31. <https://doi.org/https://doi.org/10.1016/B978-0-12-818411-0.00009-4>.
- [3] W. Li, S. Karnati, C. Kriewall, F. Liou, J. Newkirk, K.M.B. Taminger, W.J. Seufzer, Fabrication and characterization of a functionally graded material from Ti-6Al-4V to SS316 by laser metal deposition, *Addit. Manuf.* 14 (2017) 95–104. <https://doi.org/https://doi.org/10.1016/j.addma.2016.12.006>.
- [4] X. Zhang, Y. Chen, F. Liou, Fabrication of SS316L-IN625 functionally graded materials by powder-fed directed energy deposition, *Sci. Technol. Weld. Join.* 24 (2019) 504–516. <https://doi.org/10.1080/13621718.2019.1589086>.
- [5] B. Onuikwe, A. Bandyopadhyay, Bond strength measurement for additively manufactured Inconel 718- GRCop84 copper alloy bimetallic joints, *Addit. Manuf.* 27 (2019) 576–585. <https://doi.org/https://doi.org/10.1016/j.addma.2019.04.003>.
- [6] L.D. Bobbio, R.A. Otis, J.P. Borgonia, R.P. Dillon, A.A. Shapiro, Z.-K. Liu, A.M. Beese, Additive manufacturing of a functionally graded material from Ti-6Al-4V to Invar: Experimental characterization and thermodynamic calculations, *Acta Mater.* 127 (2017) 133–142. <https://doi.org/https://doi.org/10.1016/j.actamat.2016.12.070>.
- [7] T.P.Y.Z.L.L.F.L. Xinchang Zhang Cheng Sun, Additive Manufacturing of Copper – H13 Tool Steel Bi-metallic Structures via Ni-based Multi-interlayer, *Addit. Manuf.* (n.d.).
- [8] I. Sen, E. Amankwah, N.S. Kumar, E. Fleury, K. Oh-ishi, K. Hono, U. Ramamurty, Microstructure and mechanical properties of annealed SUS 304H austenitic stainless steel with copper, *Mater. Sci. Eng. A.* 528 (2011) 4491–4499. <https://doi.org/https://doi.org/10.1016/j.msea.2011.02.019>.
- [9] S. V Gladkovsky, S. V Kuteneva, S.N. Sergeev, Microstructure and mechanical properties of sandwich copper/steel composites produced by explosive welding, *Mater. Charact.* 154 (2019) 294–303. <https://doi.org/https://doi.org/10.1016/j.matchar.2019.06.008>.
- [10] S. Chen, J. Huang, J. Xia, X. Zhao, S. Lin, Influence of processing parameters on the characteristics of stainless steel/copper laser welding, *J. Mater. Process. Technol.* 222 (2015) 43–51. <https://doi.org/https://doi.org/10.1016/j.jmatprotec.2015.03.003>.
- [11] H. Sabetghadam, A.Z. Hanzaki, A. Araee, Diffusion bonding of 410 stainless steel to copper using a nickel interlayer, *Mater. Charact.* 61 (2010) 626–634. <https://doi.org/https://doi.org/10.1016/j.matchar.2010.03.006>.
- [12] J. Kar, S.K. Roy, G.G. Roy, Effect of beam oscillation on electron beam welding of

- copper with AISI-304 stainless steel, *J. Mater. Process. Technol.* 233 (2016) 174–185. <https://doi.org/https://doi.org/10.1016/j.jmatprotec.2016.03.001>.
- [13] C. Tan, K. Zhou, W. Ma, L. Min, Interfacial characteristic and mechanical performance of maraging steel-copper functional bimetal produced by selective laser melting based hybrid manufacture, *Mater. Des.* 155 (2018) 77–85. <https://doi.org/https://doi.org/10.1016/j.matdes.2018.05.064>.
- [14] A. Mannucci, I. Tomashchuk, V. Vignal, P. Sallamand, M. Duband, Parametric study of laser welding of copper to austenitic stainless steel, *Procedia CIRP.* 74 (2018) 450–455. <https://doi.org/https://doi.org/10.1016/j.procir.2018.08.160>.
- [15] S. V Kuryntsev, A.E. Morushkin, A.K. Gilmudtinov, Fiber laser welding of austenitic steel and commercially pure copper butt joint, *Opt. Lasers Eng.* 90 (2017) 101–109. <https://doi.org/https://doi.org/10.1016/j.optlaseng.2016.10.008>.
- [16] S. Chen, J. Huang, J. Xia, H. Zhang, X. Zhao, Microstructural characteristics of a stainless steel/copper dissimilar joint made by laser welding, *Metall. Mater. Trans. A Phys. Metall. Mater. Sci.* 44 (2013) 3690–3696. <https://doi.org/10.1007/s11661-013-1693-z>.
- [17] Q. Nguyen, A. Azadkhou, M. Akbari, A. Panjehpour, A. Karimipour, Experimental investigation of temperature field and fusion zone microstructure in dissimilar pulsed laser welding of austenitic stainless steel and copper, *J. Manuf. Process.* 56 (2020) 206–215. <https://doi.org/https://doi.org/10.1016/j.jmapro.2020.03.037>.
- [18] C.-H. Shiau, M.D. McMurtrey, R.C. O'Brien, N.D. Jerred, R.D. Scott, J. Lu, X. Zhang, Y. Wang, L. Shao, C. Sun, Deformation behavior and irradiation tolerance of 316 L stainless steel fabricated by direct energy deposition, *Mater. Des.* 204 (2021) 109644. <https://doi.org/https://doi.org/10.1016/j.matdes.2021.109644>.
- [19] B. Zhang, L. Dembinski, C. Coddet, The study of the laser parameters and environment variables effect on mechanical properties of high compact parts elaborated by selective laser melting 316L powder, *Mater. Sci. Eng. A.* 584 (2013) 21–31. <https://doi.org/10.1016/j.msea.2013.06.055>.
- [20] X. Zhang, T. Pan, Y. Chen, L. Li, Y. Zhang, F. Liou, Additive manufacturing of copper-stainless steel hybrid components using laser-aided directed energy deposition, *J. Mater. Sci. Technol.* 80 (2021) 100–116. <https://doi.org/https://doi.org/10.1016/j.jmst.2020.11.048>.
- [21] X. Lin, T.M. Yue, Phase formation and microstructure evolution in laser rapid forming of graded SS316L / Rene88DT alloy, *Mater. Sci. Eng. A.* 402 (2005) 294–306. <https://doi.org/10.1016/j.msea.2005.05.024>.
- [22] Y. Huang, M. Ansari, H. Asgari, M.H. Farshidianfar, D. Sarker, M.B. Khamesee, E. Toyserkani, Rapid prediction of real-time thermal characteristics, solidification parameters and microstructure in laser directed energy deposition (powder-fed additive manufacturing), *J. Mater. Process. Technol.* 274 (2019) 116286. <https://doi.org/https://doi.org/10.1016/j.jmatprotec.2019.116286>.
- [23] X. Zhang, L. Li, T. Pan, Y. Chen, Y. Zhang, W. Li, F. Liou, Additive manufacturing of copper-tool steel dissimilar joining: Experimental characterization and thermal modeling, *Mater. Charact.* (2020) 110692. <https://doi.org/https://doi.org/10.1016/j.matchar.2020.110692>.
- [24] A. Popovich, V. Sufiiarov, I. Polozov, E. Borisov, D. Masaylo, A. Orlov, Microstructure and mechanical properties of additive manufactured copper alloy, *Mater. Lett.* 179 (2016) 38–41. <https://doi.org/https://doi.org/10.1016/j.matlet.2016.05.064>.

- [25] Z.H. Liu, D.Q. Zhang, S.L. Sing, C.K. Chua, L.E. Loh, Interfacial characterization of SLM parts in multi-material processing: Metallurgical diffusion between 316L stainless steel and C18400 copper alloy, *Mater. Charact.* 94 (2014) 116–125. <https://doi.org/https://doi.org/10.1016/j.matchar.2014.05.001>.
- [26] B. Yun, W.C. B, An exploration of binder jetting of copper, *Rapid Prototyp. J.* 21 (2015) 177–185. <https://doi.org/10.1108/RPJ-12-2014-0180>.
- [27] K. Yang, W. Li, X. Guo, X. Yang, Y. Xu, Characterizations and anisotropy of cold-spraying additive-manufactured copper bulk, *J. Mater. Sci. Technol.* 34 (2018) 1570–1579. <https://doi.org/https://doi.org/10.1016/j.jmst.2018.01.002>.
- [28] J. Butt, H. Mebrahtu, H. Shirvani, Microstructure and mechanical properties of dissimilar pure copper foil/1050 aluminium composites made with composite metal foil manufacturing, *J. Mater. Process. Technol.* 238 (2016) 96–107. <https://doi.org/https://doi.org/10.1016/j.jmatprotec.2016.07.014>.
- [29] S.C. Krishna, K. V Radhika, K. Thomas Tharian, G. Sudarshan Rao, M. Swathi Kiranmayee, B. Pant, Effect of Simulated Brazing Cycle on the Microstructure and Mechanical Properties of Cu-Cr-Zr-Ti Alloy, *Mater. Sci. Forum.* 710 (2012) 626–631. <https://doi.org/10.4028/www.scientific.net/MSF.710.626>.
- [30] D.R. Feenstra, A. Molotnikov, N. Birbilis, Effect of energy density on the interface evolution of stainless steel 316L deposited upon INC 625 via directed energy deposition, *J. Mater. Sci.* 55 (2020) 13314–13328. <https://doi.org/10.1007/s10853-020-04913-y>.